Supplementary information for ultra-fast photochemistry in the strong light-matter coupling regime

Arpan Dutta[1,4], Ville Tiainen[1], Luís Duarte[1,3], Nemanja Markešević[1], Dmitry Morozov[2], Hassan A. Qureshi[1,4], Gerrit Groenhof[2,*], and J. Jussi Toppari[1,*]

[1] *Nanoscience Center and Department of Physics, University of Jyväskylä, P.O. Box 35, FI-40014, Finland*
[2] *Nanoscience Center and Department of Chemistry, University of Jyväskylä, P.O. Box 35, FI-40014, Finland*
[3] *Present address: Department of Chemistry, University of Helsinki, P.O. Box 55, FI-00014, Finland*
[4] *Present address: Department of Mechanical and Materials Engineering, University of Turku, FI-20014, Finland*
[*] *Correspondence: j.jussi.toppari@jyu.fi gerrit.x.groenhof@jyu.fi*

Contents

1 Experiments with metallic Fabry-Pérot cavities containing HBQ molecules

1.1 Optical microcavity design

Our molecular films used as a reference consist of a 100 nm thick polymer layer on top of a 120 nm thick aluminum (Al) mirror on a glass substrate. The polymer layer is a polymethyl methacrylate (PMMA) matrix doped with 10-hydroxybenzo[h]quinoline (HBQ) molecules, purchased from TCI Europe N.V. (Belgium, CAS Number: 33155-90-7, Molecular Weight: 195.22 g/mol) and used as received. In the case of cavities, we added a 20 nm Al mirror on top of the film. This yields a low-Q ($Q \approx 17$) all-metal Fabry-Pérot microcavity with an asymmetric geometry having a thin/leaky mirror (20 nm Al) on top and a thick/non-transparent (120 nm Al) mirror at the bottom. The structures of the HBQ film and cavity are schematically shown in Fig. S1.

We optimized our cavity geometry using transfer-matrix method (TMM) [S1, S2] and finite-difference time-domain (FDTD) [S3, S4] simulations. In TMM calculations, the glass substrate (SiO_2) and the surrounding medium (air, refractive index 1.00) were considered as semi-infinite. The excitation light was s-polarized and the refractive index of PMMA was 1.50. The material models for Al and SiO_2 were taken from the existing literature [S5]. In 2D-FDTD computations, the simulations were carried out on xz-plane considering the cavity and the film thickness extending in z-direction while in x- and y-directions, the structures are uniform. Perfectly matched layers (PML) were used in all boundaries and the material models were the same that were used for the TMM. The normal incidence of light, *i.e.*, a plane wave linearly polarized in x/y direction was used as the excitation in the simulations.

We chose a reflective (non-transmissive) cavity since that can provide an efficient light confinement combined with a quality detection of molecular fluorescence [S6]. The cavity thickness was set to 100 nm to tune the first order cavity mode with the HBQ absorption (375 nm) at 0° excitation. However, considering the fabrication tolerance, the actual cavity thickness was $\sim 100 - 120$ nm resulting in the resonant tuning around 40° due to the cavity dispersion.

The TMM calculated absorption of the undoped cavity and film with pure PMMA as a polymer layer, are reported in Fig. S2(a) for 40° excitation angle. The TMM computed dispersion of the undoped cavity is depicted in Fig. S2(b). The 2D-FDTD simulated spatial distribution of the electric-field inside the undoped cavity and film are depicted in Fig. S2(c) and Fig. S2(d), respectively, at resonance (375 nm) for the normal incidence of light. Unlike for the cavity, no field-confinement was found in the film.

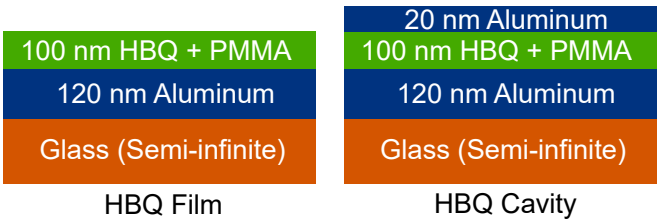

Fig. S1. Schematics of HBQ film and cavity.

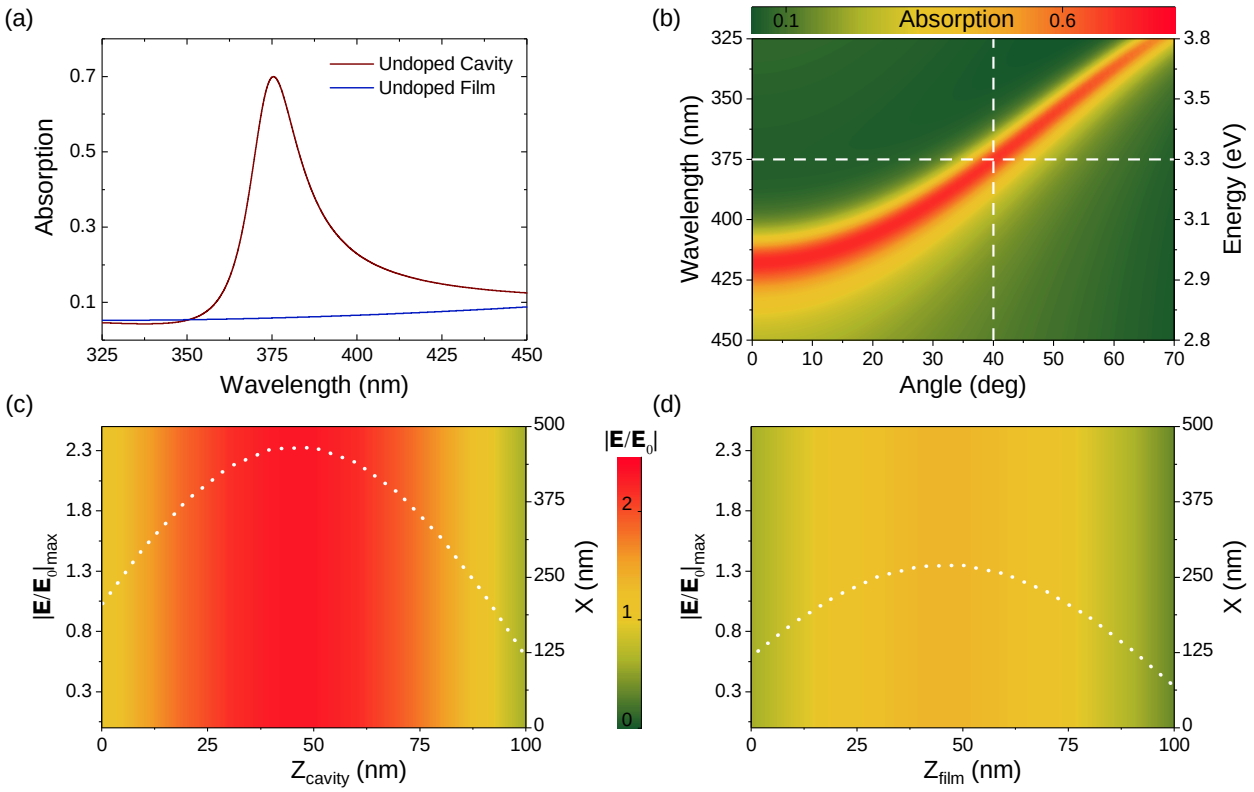

Fig. S2. (a) Absorption of the undoped cavity and film at 40° excitation angle. (b) Dispersion of the undoped cavity where the horizontal and vertical white dashed lines show the HBQ absorption (375 nm) and the resonant angle at which the first order cavity mode is at 375 nm, respectively. Spatial distribution of the electric field at 375 nm inside the undoped (c) cavity and (d) film shown as a color contour plot. Since the field is homogeneous in x-direction, the white dotted curves with their scale at left axis show the spatial profile of the electric field inside the corresponding structures.

1.2 Sample fabrication

HBQ films and cavities were fabricated on top of BK7 glass substrates (Präzisions Glas and Optik GmbH, dimension: $15 \times 15\,\mathrm{mm}^2$, thickness: 1 mm). The substrates were cleaned with heated acetone and sonication in isopropanol followed by drying by nitrogen flow. The bottom mirrors for the films and cavities were made by evaporating 120 nm of Al on top of the cleaned substrates in ultra high vacuum (e-beam evaporation with depostion rate 0.1 nm/s under $10^{-8} - 10^{-9}$ mbar pressure). The yellow crystalline HBQ powder (TCI Europe N.V.) was dissolved in chlorobenzene at room temparature to make a 8 wt% stock solution of HBQ. The spin solutions were prepared by mixing the required amount of 2 wt% solution of PMMA in chlorobenzene (950PMMA C2, Microchem) with the 8 wt% stock solution of HBQ to attain the target concentrations, i.e., HBQ:PMMA ratios 0.5 (low), 1 (mid), and 1.6 (high). The HBQ:PMMA thin films were made by spin-coating the bottom mirrors with the spin solution at an optimal spin speed to achieve $\sim 100 - 120$ nm film thickness. The obtained films were baked for 15 min on a hot plate at 65°C. The temperature was lowered from the common PMMA baking temperature to avoid excess evaporation of HBQ. The

thickness characterization was performed using the KLA Tencor P-15 profilometer. For each concentration, two identical HBQ:PMMA films were prepared - one for cavity and one for corresponding film. For cavities, the top mirrors were made by evaporating 20 nm of Al on top of the HBQ:PMMA films under the same evaporation conditions as for the bottom mirrors. The undoped cavity was made using the similar procedure except the HBQ doping.

1.3 Steady-state reflection measurements

The reflection measurements on the fabricated samples were carried out using a custom made optical setup shown schematically in Fig. S3. The samples were illuminated by a deuterium lamp (Cathodeon, model C710). The pseudo-collimated excitation light passed two pinholes P_1 and P_2 having diameters of ~ 6 mm and ~ 3 mm, respectively, before hitting the sample. The samples were placed at the rotation axis of a goniometric sample stage facing the excitation light with the axis of the prism polarizer along with the rotation axis, i.e., vertical or s-polarization. The excitation (θ) and detection (ϕ) angles were adjusted manually by rotating the goniometric stage and the rotational arm, respectively. For reflection measurements eventually $\theta = \phi$ and θ ranges from 10° to 70° with an increment of 5°. The reflection spectra of the samples were collected using a fiber coupler (ThorLabs F220SMA-A, f = 10.90 mm, NA = 0.25) connected to an optical fiber (ThorLabs, model: M112L02, 2 m, 200 µm core, NA = 0.22, SMA). The collected light was guided to a spectrometer consisting of a monochromator (Acton monochromator SP2150i, slit size: 100 µm, grating: 600 grooves/mm blazed at 500 nm) and CCD (Andor InstaSpec IV CCD DU420-OE, pixel size: 16×16 µm^2). The obtained spectra were recorded in ASCII format.

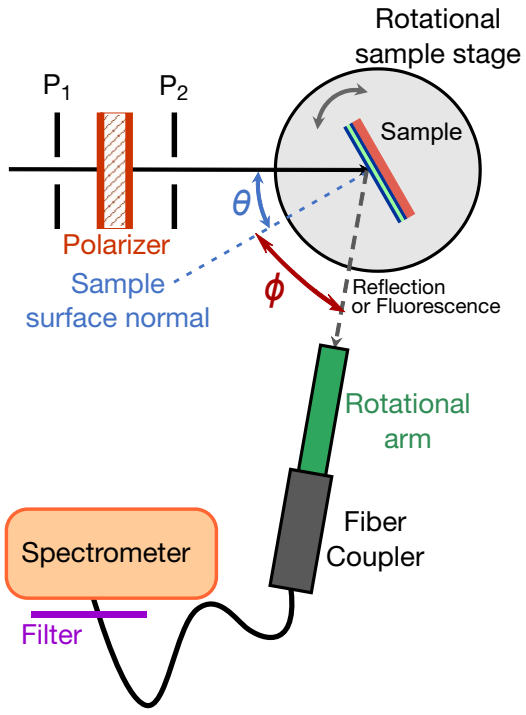

Fig. S3. Schematic of the experimental set-up.

The angle-resolved reflection spectra $R(\theta, \lambda)$ were calculated as $R(\theta, \lambda) = I(\theta, \lambda)/I_0(\lambda)$, where $I(\theta, \lambda)$ is the collected signal (in counts) reflected from the sample while $I_0(\lambda)$ is the lamp spectrum. Since our samples are non-transmissive, *i.e.*, $T(\theta, \lambda) = 0$, the absorption can be calculated simply as $1 - R(\theta, \lambda)$. First, we estimated the scattered part of the excitation light that never reached to the HBQ molecules embedded in our samples due to scattering from polymer/top mirror using a baseline correction. The baseline-correction is done by interpolating the baseline in between the known baseline points in MATLAB [S7]. The interpolation was done by using a MATLAB function *interp1* [S8] along with the piecewise cubic Hermite polynomial method implemented through the MATLAB function *pchip* [S9]. The trend in baseline was similar in almost all cases, *i.e.*, raising baseline towards blue. This is exactly something one would expect from a nonspecular Rayleigh scattering from a rough sample surface, which is the main reason for the non-zero baseline. It should be noted that many interpolation methods as well as parameters were tested, and all of them yielded the same trend as reported in the main text.

Finally, the angle-dependent absorption spectra $A(\theta, \lambda)$ were considered as

$$A(\theta, \lambda) = 1 - \frac{I(\theta, \lambda)}{I_0(\lambda) - [I_0(\lambda) \times BL(\lambda)]}$$

where $BL(\lambda)$ is the estimated baseline.

The measured dispersion of a fabricated undoped cavity is reported in Fig. S4 which is consistent with our simulated dispersion shown in Fig. S2(b) except for the fact that the fabricated cavity thickness is $\sim$ 118 nm resulting in the resonant tuning of the first order cavity mode with 375 nm at 50°, i.e., 10° detuning from the simulated case due to a higher thickness.

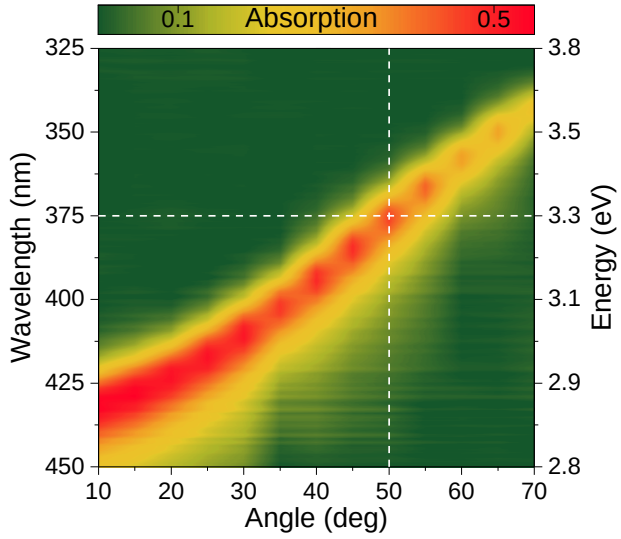

Fig. S4. Measured dispersion of a fabricated undoped cavity where the horizontal and vertical white dashed lines show the HBQ absorption (375 nm) and the resonant angle at which the first order cavity mode is at 375 nm, respectively.

The angle-dependent absorption spectra after baseline correction for low, mid, and high concentration (C) cavities are illustrated in Figs. S5(a), S5(c), and Fig. S5(e), respectively. The same without baseline correction for low, mid, and high C cavities are presented in Figs. S5(b), S5(d), and Fig. S5(f), respectively. From Fig. S5 it is clear that the resonant condition in all cavities appears close to 40° angle.

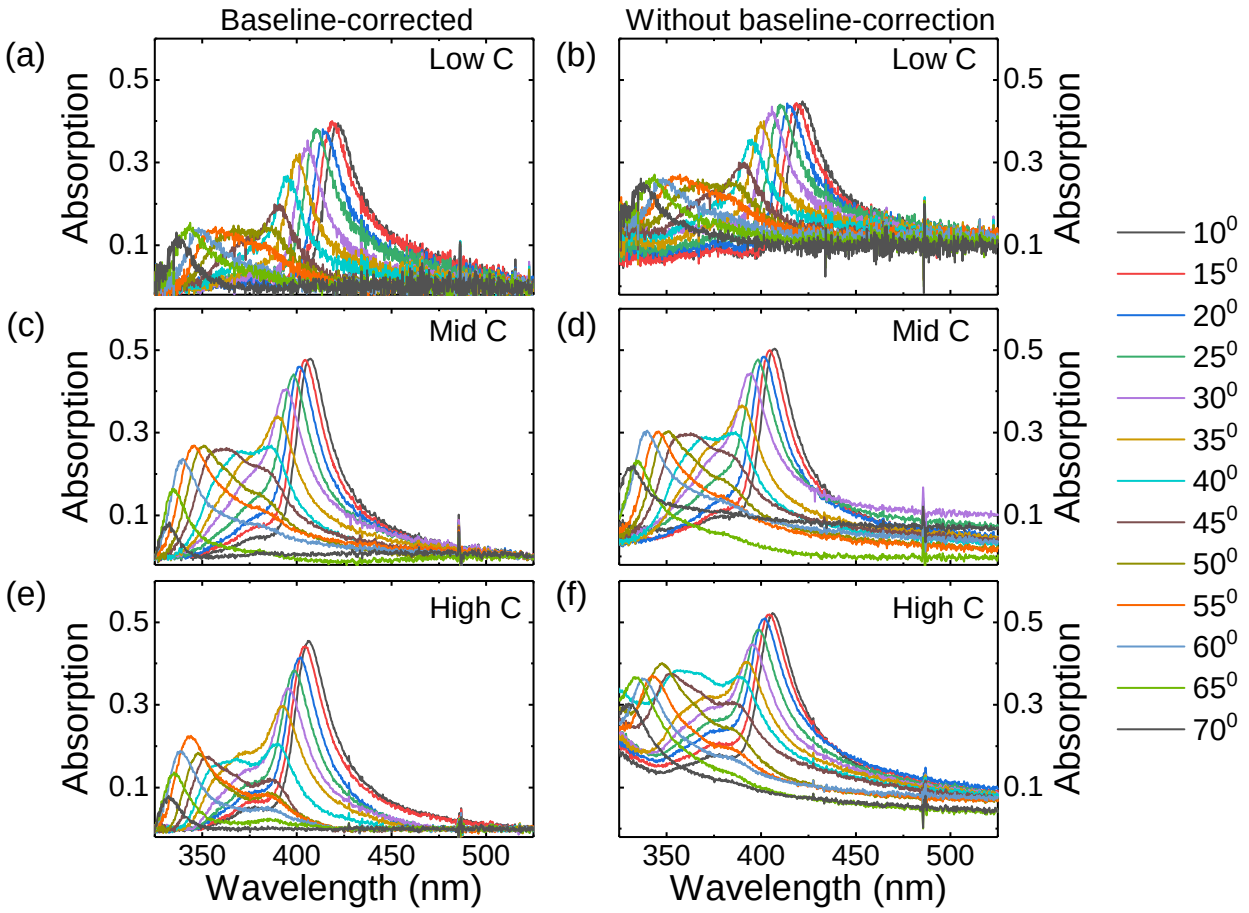

Fig. S5. Angle-dependent absorption spectra for (a) low, (c) mid, and (e) high C cavities after baseline correction. The same for (b) low, (d) mid, and (f) high C cavities without baseline correction.

1.4 Steady-state fluorescence measurements

In fluorescence studies, the fabricated samples were excited by a tunable diode pumped pulse laser (EKSPLA OPO NT230 series, model: NT231-100-SH/FH-OPO-SH, pulse width: 3 - 6 ns, repetition rate: 100 Hz) where the excitation beam was pseudo-collimated before reaching the samples. The sample positioning on the rotational stage, the polarization axis, the adjustment of the excitation/detection angles, and the pinhole sizes were identical with the reflection measurements. For cavities, five excitation angles were considered, *i.e.*, θ as 10°, 30°, 40°, 50° and 60°. The detection angle ϕ was set to 0° for all θ except for $\theta = 10°$ where ϕ was set to 30° to avoid the reflection of the incident laser light at the detector. For

films, θ was 30° with ϕ as 0° since there is no dispersion. The sample emission was collected using the same fiber coupler used in the reflectivity measurements connected to a fiber optic bundle (ThorLabs, model: BFL200HS02, 250 to 1200 nm, 7×200 µm core fibers, high-OH, SMA). The collected light was guided to a monochromator (Acton monochromator SP2150i, slit size: 750 µm, grating: 300 grooves/mm blazed at 750 nm) – CCD (Andor IVAC CCD DR-324B-FI, pixel size: 16×16 µm^2) combination and recorded in ASCII format. The filter before the spectrometer shown in Fig. S3 (Semrock EdgeBasic, BLP01-488R-25 long pass filter, transparency: ≥ 488 nm) was only used in the fluorescence measurements to block the excitation light during emission collection. To take into account the typical fluctuations in the pulse energy of our excitation laser, we recorded the energy of each excitation pulse using a sensor (Ophir PD10-C) and used the sum of energies of all excitation pulses to correct the collected emission intensity (in counts).

The energy-corrected emission spectra $I_E(\lambda)$ in counts/mJ were calculated as $I_E(\lambda) = I_C(\lambda)/\sum E_P$ where $I_C(\lambda)$ is the collected emission in counts and $\sum E_P$ represents the sum of energies of all excitation pulses in mJ during the detection/integration time. The exciation spectra were constructed by extracting the energy-corrected emission intensities at 620 nm, i.e., $I_E(\lambda = 620\,\text{nm})$ as a function of excitation wavelengths (λ_{ex}) where λ_{ex} was varied from 350 - 400 nm with an increment of 3 nm.

1.5 Coupled harmonic oscillator model fitting

The probabilities of polariton formation in a strongly-coupled cavity-molecular system are given by the Hopfield coefficients [S10]. In order to extract those coefficients from the experimental data, the coupled harmonic oscillator model (CHOM) [S11, S12] was fitted to the experimental polariton dispersions. In the case of two excitons the coupling is described by a 3×3 matrix of regular James-Cummings Hamiltonian

$$\begin{pmatrix} E_c(k_\parallel) & g_1 & g_2 \\ g_1 & E_1 & 0 \\ g_2 & 0 & E_2 \end{pmatrix} \begin{pmatrix} \alpha \\ \beta \\ \gamma \end{pmatrix} = E \begin{pmatrix} \alpha \\ \beta \\ \gamma \end{pmatrix}, \tag{S.1}$$

where g_1 and g_2 are the coupling strengths related to the molecular excitation energies, the molecular exciton at $E_1 = 3.30$ eV (375 nm) and the vibronic shoulder at $E_2 = 3.44$ eV (360 nm), respectively. In Eq. (S.1), α, β, and γ are the Hopfield coefficients and $E_c(k_\parallel)$ is the cavity energy given by

$$E_c(k_\parallel) = \frac{\hbar c}{n_c} \sqrt{\left(\frac{\pi}{L}\right)^2 + k_\parallel^2}, \tag{S.2}$$

where n_c is the refractive index of the cavity medium and L is the cavity thickness. The in-plane wave vector $k_\parallel$ is given by

$$k_\parallel = \frac{2\pi}{\lambda} \sin\theta, \tag{S.3}$$

where λ is the wavelength and θ is the angle of incidence relative to the cavity surface normal [S11, S12].

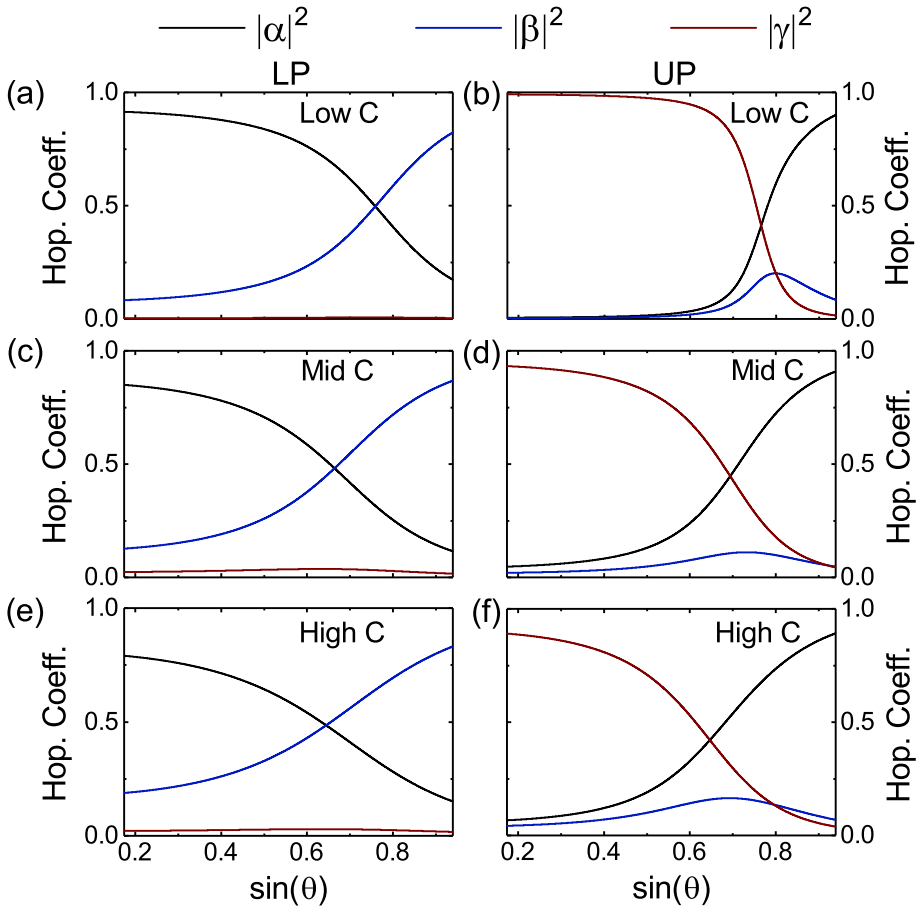

Fig. S6. Hopfield coefficients of the lower polariton (LP) branch for (a) low, (c) mid, and (e) high concentration (C) HBQ cavities. Hopfield coefficients of the upper polariton (UP) branch for (b) low, (d) mid, and (f) high C HBQ cavities. In (a)-(f), the relative coefficients are calculated from the CHOM fitting.

A custom made MATLAB script was used to fit Eq. (S.1) to the experimental data. To obtain the fit parameters g_1, g_2, n_c and L were varied until the difference between experimental polariton energies and the ones obtained from Eq. (S.1) was minimized. The method of least squares was used to define the minimum. Experimental polariton energies were extracted from the measured cavity absorption maxima, by fitting a suitable peak functions corresponding to the three polaritons, and the corresponding incident angles were converted to $k_{||}$ for the purposes of fitting. The fitted dispersion curves for all samples are shown together with the measured data in Fig. 2 of the main article, and the corresponding Hopfield coefficients are presented in Fig. S6.

2 Molecular Dynamics of HBQ in the collective strong coupling regime

2.1 Multi-scale Tavis-Cummings model

To model the dynamics of N HBQ molecules strongly coupled to the confined light mode of a single-mode cavity, we extended the Tavis-Cummings model [S13, S14] to account for the molecular degrees of freedom [S15]:

$$\begin{aligned} \hat{H}^{\mathrm{TC}} &= \textstyle\sum_j^N h\nu_j(\mathbf{R}_j)\hat{\sigma}_j^+\hat{\sigma}_j^- + \hbar\omega_{\mathrm{cav}}\hat{a}^\dagger\hat{a} + \\ & \textstyle\sum_j^N \hbar g_j(\hat{\sigma}_j^+\hat{a} + \hat{\sigma}_j^-\hat{a}^\dagger) + \\ & \textstyle\sum_i^N V_{\mathrm{S}_0}^{\mathrm{mol}}(\mathbf{R}_i) \end{aligned} \tag{S.1}$$

Here, $\hat{\sigma}_j^+$ ($\hat{\sigma}_j^-$) is the operator that excites (de-excites) HBQ molecule j from the electronic ground (excited) state $|\mathrm{S}_0^j(\mathbf{R}_j)\rangle$ ($|\mathrm{S}_1^j(\mathbf{R}_j)\rangle$) into the electronic excited (ground) state $|\mathrm{S}_1^j(\mathbf{R}_j)\rangle$ ($|\mathrm{S}_0^j(\mathbf{R}_j)\rangle$); $\mathbf{R}_j$ is the vector of the Cartesian coordinates of all atoms in HBQ molecule j; $\hat{a}$ ($\hat{a}^\dagger$) is the annihilation (creation) operator of an excitation in the cavity mode; $h\nu_j(\mathbf{R}_j)$ is the excitation energy of molecule j, defined as:

$$h\nu_j(\mathbf{R}_j) = V_{\mathrm{S}_1}^{\mathrm{mol}}(\mathbf{R}_j) - V_{\mathrm{S}_0}^{\mathrm{mol}}(\mathbf{R}_j) \tag{S.2}$$

with $V_{\mathrm{S}_0}^{\mathrm{mol}}(\mathbf{R}_j)$ and $V_{\mathrm{S}_1}^{\mathrm{mol}}(\mathbf{R}_j)$ the adiabatic potential energy surfaces of molecule j in the electronic ground (S_0) and excited (S_1) state, respectively.

The last term in Equation S.1 is the total potential energy of the system in the absolute ground state (*i.e.*, with no excitations in neither the molecules nor the cavity modes), defined as the sum of the ground-state potential energies of all molecules in the cavity. The $V_{\mathrm{S}_0}^{\mathrm{mol}}(\mathbf{R}_j)$ and $V_{\mathrm{S}_1}^{\mathrm{mol}}(\mathbf{R}_j)$ adiabatic potential energy surfaces are modelled at the QM/MM level of theory [S16, S17].

The third term in Equation S.1 models the light-matter interaction within the dipolar approximation through g_j:

$$g_j = -\boldsymbol{\mu}_j^{\mathrm{TDM}}(\mathbf{R}_j)\cdot\mathbf{u}_{\mathrm{cav}}\sqrt{\frac{\hbar\omega_{\mathrm{cav}}}{2\epsilon_0 V_{\mathrm{cav}}}} \tag{S.3}$$

where $\boldsymbol{\mu}_j^{\mathrm{TDM}}(\mathbf{R}_j)$ is the transition dipole moment of HBQ molecule j that depends on the molecular geometry ($\mathbf{R}_j$); $\mathbf{u}_{\mathrm{cav}}$ the unit vector in the direction of the electric component of the cavity vacuum field (*i.e.*, $|\mathbf{E}| = \sqrt{\hbar\omega_{\mathrm{cav}}(k_z)/2\epsilon_0 V_{\mathrm{cav}}}$); ϵ_0 the vacuum permittivity; and V_{cav} the cavity mode volume.

The matrix elements of the multi-scale Tavis-Cummings Hamiltonian are evaluated in the product basis of adiabatic molecular states times cavity mode excitation:

$$\begin{aligned} |\phi_j\rangle &= \hat{\sigma}_j^+|\mathrm{S}_0^1\mathrm{S}_0^2..\mathrm{S}_0^{N-1}\mathrm{S}_0^N\rangle\otimes|0\rangle \\ &= \hat{\sigma}_j^+|\Pi_i^N\mathrm{S}_0^i\rangle\otimes|0\rangle \\ &= \hat{\sigma}_j^+|\phi_0\rangle \end{aligned} \tag{S.4}$$

for $1 \leq j \leq N$, and

$$\begin{aligned} |\phi_{N+1}\rangle &= \hat{a}^\dagger |\mathrm{S}_0^1 \mathrm{S}_0^2 .. \mathrm{S}_0^{N-1} \mathrm{S}_0^N\rangle \otimes |0\rangle \\ &= \hat{a}^\dagger |\Pi_i^N \mathrm{S}_0^i\rangle \otimes |0\rangle \\ &= \hat{a}^\dagger |\phi_0\rangle \end{aligned} \tag{S.5}$$

In these expressions $|0\rangle$ indicates that the Fock state of the cavity mode is empty. The basis state $|\phi_0\rangle$ is the ground state of the molecule-cavity system with no excitations in neither the molecules nor the cavity mode:

$$|\phi_0\rangle = |\mathrm{S}_0^1 \mathrm{S}_0^2 .. \mathrm{S}_0^{N-1} \mathrm{S}_0^N\rangle \otimes |0\rangle = |\Pi_i^N \mathrm{S}_0^i\rangle \otimes |0\rangle \tag{S.6}$$

Within this basis, the Matrix representation of the Tavis-Cummings matrix becomes:

$$\mathbf{H}^{\mathrm{TC}} = \begin{pmatrix} \mathbf{H}^{\mathrm{mol}} & \mathbf{H}^{\mathrm{int}} \\ \mathbf{H}^{\mathrm{int}\dagger} & H^{\mathrm{cav}} \end{pmatrix} \tag{S.7}$$

The upper left block, $\mathbf{H}^{\mathrm{mol}}$, is an $N \times N$ matrix that contains the single-photon excitations of the molecules. Because we neglect direct excitonic interactions between molecules, this block is diagonal, with elements labeled by the molecule indices j:

$$H_{j,j}^{\mathrm{mol}} = \langle \phi_0 | \hat{\sigma}_j \hat{H}^{\mathrm{TC}} \hat{\sigma}_j^+ | \phi_0 \rangle \tag{S.8}$$

for $1 \leq j \leq N$. Each matrix element of $\mathbf{H}^{\mathrm{mol}}$ thus represents the potential energy of a HBQ molecule, j, in the electronic excited state $|\mathrm{S}_1^j(\mathbf{R}_j)\rangle$ while all other molecules, $i \neq j$, are in the electronic ground state $|\mathrm{S}_0^i(\mathbf{R}_i)\rangle$:

$$H_{j,j}^{\mathrm{mol}} = V_{\mathrm{S}_1}^{\mathrm{mol}}(\mathbf{R}_j) + \sum_{i \neq j}^{N} V_{\mathrm{S}_0}^{\mathrm{mol}}(\mathbf{R}_i) \tag{S.9}$$

The lower right diagonal element in Equation S.7, $\mathbf{H}^{\mathrm{cav}}$, represents the single-photon excitation of the cavity mode,:

$$H_{N+1,N+1}^{\mathrm{cav}} = \langle \phi_0 | \hat{a} \hat{H}^{\mathrm{TC}} \hat{a}^\dagger | \phi_0 \rangle \tag{S.10}$$

In these matrix elements, all HBQ molecules are in the electronic ground state (S_0). The energy is therefore the sum of the cavity energy at $k_{z,p}$, and the molecular ground state energies:

$$H_{N+1,N+1}^{\mathrm{cav}} = \hbar\omega_{\mathrm{cav}} + \sum_{j}^{N} V_{\mathrm{S}_0}^{\mathrm{mol}}(\mathbf{R}_j) \tag{S.11}$$

where ω_{cav} is the cavity frequency.

The two N dimensional off-diagonal vectors $\mathbf{H}^{\mathrm{int}}$ and $\mathbf{H}^{\mathrm{int}\dagger}$ in the Tavis-Cummings Hamiltonian (Equation S.7) model the light-matter interactions between the HBQ molecules and

the cavity mode. The elements of these vectors are approximated as the inner product between the molecular transition dipole moments on the one hand, and the transverse electric field of the cavity mode at the center of the molecules, on the other hand:

$$\begin{aligned} H^{\text{int}}_{j,N+1} &= -\mu^{\text{TDM}}_j(\mathbf{R}_j)\cdot\mathbf{u}_{\text{cav}}\sqrt{\tfrac{\hbar\omega_{\text{cav}}}{2\epsilon_0 V_{\text{cav}}}}\langle\phi_0|\hat{\sigma}_j(\hat{\sigma}^+_j\hat{a})\hat{a}^\dagger|\phi_0\rangle \\ &= -\mu^{\text{TDM}}_j(\mathbf{R}_j)\cdot\mathbf{u}_{\text{cav}}\sqrt{\tfrac{\hbar\omega_{\text{cav}}}{2\epsilon_0 V_{\text{cav}}}} \end{aligned} \tag{S.12}$$

Diagonalization of the multi-scale Tavis-Cummings Hamiltonian in Equation S.7 yields the $N+1$ eigenstates $|\psi^m\rangle$:

$$|\psi^m\rangle = \left(\sum_j^N \beta^m_j\hat{\sigma}^+_j + \alpha^m\hat{a}^\dagger\right)|\phi_0\rangle \tag{S.13}$$

with eigenenergies E_m. Expansion coefficients β^m_j and α^m reflect the contribution of the molecular excitons ($|\mathrm{S}^j_1(\mathbf{R}_j)\rangle$) and the cavity mode excitation ($|1\rangle$) to eigenstate $|\psi^m\rangle$, respectively.

2.2 Non-adiabatic molecular dynamics simulations

MD trajectories of all molecules (including environment) were computed by numerically integrating Newton's equations of motion. The multi-mode Tavis-Cummings Hamiltonian (Equation S.7) was diagonalized at each time-step of the simulation to obtain the $N+1$ (adiabatic) eigenstates $|\psi^m\rangle$ and energies E^m. The trajectories were evolved on the PES of a *single* eigenstate, $|\psi^m\rangle$:

$$V({}_m\mathbf{R} = \langle\psi^m|\hat{H}^{\text{TC}}|\psi^m\rangle \tag{S.14}$$

Population transfers between states were modelled with a surface hopping method [S18].

The surface hopping algorithm used in this work [S19] is based on the Landau-Zener model [S20, S21], which relates the probability of a transition between two adiabatic states $|\psi_k\rangle$ and $|\psi_m\rangle$ to the non-adiabatic coupling, via:

$$P_{k\to m} = \exp[-\frac{1}{4}\pi\xi] \tag{S.15}$$

with ξ the Massey parameter, defined as [S22]:

$$\xi = \frac{\Delta E_{km}}{\hbar\langle\psi^k|\frac{\partial}{\partial t}\psi^m\rangle} \tag{S.16}$$

Following Hammes-Schiffer and Tully [S23] we approximate the non-adiabatic coupling $\langle\psi^k|\frac{\partial}{\partial t}\psi^m\rangle$ as $\langle\psi^k(t)|\psi^m(t+\Delta t)\rangle/\Delta t$, *i.e.*, the overlap between the state $|\psi^k\rangle$ at the current time step and the state $|\psi_m\rangle$ at the previous time step. Under the additional assumption that the uncoupled molecular wave functions vary slowly, we can further approximate this overlap as the inner product of the eigenvectors of the Tavis-Cummings matrix (Equation S.7):

$$\langle\psi^k(t)|\psi^m(t+\Delta t)\rangle = \sum_i^N \beta^k_i(t)\beta^m_i(t+\Delta t) + \alpha^k(t)\alpha^m(t+\Delta t) \tag{S.17}$$

Calculating this overlap and the energy gap ΔE_{km} at every time step is straightforward and we can use the Landau-Zener formula to calculate the probability of a transition to the other surface (equation S.15). In principle, this transition probability could be used to spawn a new trajectory on the other polaritonic surface, but since this procedure would lead to multiple trajectories that have to computed simultaneously, spawning will be too demanding in practice, in particular when there are many molecules. Instead, we restricted hopping to situations where the transition probability approaches unity. This happens when the states $|\psi^k\rangle$ and $|\psi^m\rangle$ are degenerate: $\Delta E_{km} \approx 0$ and $\langle\psi^k(t)|\psi^m(t+\Delta t)\rangle > \langle\psi^m(t)|\psi^k(t+\Delta t)\rangle$.

2.3 Simulation details

The Gromos-2016H66 force field was used to model the interactions, because it contains a validated cyclohexane model [S24], which was used as the solvent for HBQ in our simulations. In this united atom representation of cyclohexane, none of the atoms carries a partial charge. Because HBQ was kept frozen during the solvent equilibration and modeled at the QM level in all other simulations, there was no need to assign partial charges to the HBQ atoms. The Gromos96 atom-types used in the simulations are `HC` for all aromatic hydrogen atoms, `C` for all carbon atoms, `NR` for the aromatic nitrogen atom, `OA` for the hydroxyl oxygen atom and `H` for the hydroxyl proton.

One HBQ molecule was placed at the center of a rectangular box that was filled with 402 cyclohexane molecules. The simulation box, which thus contained 2436 atoms, was equilibrated for 100 ns. During equilibration, the coordinates of the HBQ atoms were kept fixed. The LINCS algorithm was used to constrain bond lengths in cyclohexane [S25] enabling a time step of 2 fs. Temperature and pressure were maintained at 300 K and 1 atmosphere by means of weak-coupling to an external bath ($\tau_T = 0.1$ ps, $\tau_P = 1$ ps) [S26]. The Lennard-Jones potential was truncated at 1.4 nm.

Snapshots were extracted from the equilibration trajectory and further equilibrated for 50 ps at the QM/MM level with a time step of 1 fs. HBQ was modelled with density functional theory (DFT), using the CAM-B3LYP functional [S27–S29] in combination with a 6-31G(d) basis set [S30]. The cyclohexane solvent was described with the 2016H66 parameter set of the Gromos96 force field [S24] The QM subsystem was mechanically embedded and because cyclohexane atoms are uncharged, the interactions between the QM and MM regions were modeled with Lennard-Jones potentials only. We used time-dependent density functional theory [S31] within the Tamm-Dancoff approximation (TDA) [S32] in combination with the CAM-B3LYP functional and the 6-31G(d) basis set, to model the singlet excited electronic (S_1) state of HBQ in our simulations. All QM/MM simulations of HBQ outside of the cavity were performed with Gromacs 4.5.3 [S33] using the QM/MM interface to TeraChem [S34, S35].

A hundred snapshots were extracted from the 50 ps ground-state trajectories and the simulations were continued in the excited state to get an estimate for the proton transfer rate outside of the cavity. For the simulations in the cavity configurations were extracted from the QM/MM ground-state trajectory and coupled to a single confined light mode with an infinite lifetime and a vacuum field strength of 0.77 MVcm^{-1} (0.00015 au). To maximize the collective coupling strength, the transition dipole moments were aligned to the cavity field. MD trajectories of 100 fs were calculated with 256 and 512 molecules in the cavity. In

these simulations, the cavity energy $\hbar\omega_{\text{cav}}$ was tuned to be in resonance with the maximum of HBQ absorption, which is 4.02 eV at the TD-CAM-B3LYP/6-31G(d)//Gromos2016H66 level of QM/MM theory. In total 22 trajectories were computed, each starting in a different polaritonic eigenstate of the HBQ-cavity system. The simulations of 512 molecules were repeated with a cavity that was red-detuned from the HBQ absorption maximum by 123 meV. All simulations were performed with Gromacs 4.5.3 [S33], in which the Tavis-Cummings Hamiltonian (Equation S.7) was implemented [S15], using the QM/MM interface to Gaussian16 [S36].

2.4 Estimation of radiative losses

To estimate the radiative loss through the imperfect cavity mirrors *a posteriori*, we coherently propagated the *total* polaritonic wavefunction $|\Psi(t)\rangle$ along the classical trajectory of the N molecules as a time-dependent superposition of the $N + n_{\text{mode}}$ time-independent adiabatic polaritonic states:

$$|\Psi(t)\rangle = \sum_{m}^{N+n_{\text{mode}}} c_m(t)|\psi^m\rangle \tag{S.18}$$

where $c_m(t)$ are the time-dependent expansion coefficients of the time-independent polaritonic basis functions $|\psi^m\rangle$ defined in Equation S.13. A unitary propagator in the *local* diabatic basis was used to integrate these coefficients [S37].

Radiative loss was modeled as a first-order decay process into the overall ground state of the system (*i.e.*, no excitation in neither the molecules nor the cavity mode) [S15]. Assuming an intrinsic decay rate of the cavity, γ_{cav}, the radiative loss rate was calculated as the product of γ_{cav} and the photonic weight, $|\alpha^m|^2$, of state $|\psi^m\rangle$ (Equation S.13). Thus, after an MD step Δt, the change in population of state $|\psi_m\rangle$, $\rho_m(t) = |c_m(t)|^2$, due to the loss is:

$$\rho_m(t + \Delta t) = \rho_m(t) \exp\left[-\gamma_{\text{cav}}|\alpha^m(t)|^2\Delta t\right] \tag{S.19}$$

Since $\rho_m = (\Re[c_m])^2 + (\Im[c_m])^2$, changes in the real and imaginary parts of the (complex) expansion coefficients $c_m(t)$ due to spontaneous photonic loss through the mirrors of a low-Q cavity, are:

$$\Re[c_m(t + \Delta t)] = \Re[c_m(t)] \exp\left[-\frac{1}{2}\gamma_{\text{cav}}|\alpha_p^m(t)|\Delta t\right]$$

$$\Im[c_m(t + \Delta t)] = \Im[c_m(t)] \exp\left[-\frac{1}{2}\gamma_{\text{cav}}|\alpha^m(t)|^2\Delta t\right]$$

In our simulations we assumed a decay rate of $\gamma_{\text{cav}} = 250$ ps^{-1}.

2.5 Cavity absorption spectra

Following Lidzey and coworkers [S38], we define the "visibility", I^m, of polaritonic state $|\psi^m\rangle$ as the photonic contribution to that state (*i.e.*, $I^m \propto |\alpha^m|^2$). Thus, the one-photon absorption spectra of the HBQ cavity systems were computed from the QM/MM trajectory of the uncoupled HBQ as follows: For each frame of this trajectory, the polaritonic states were computed and the energy gaps of these states with respect to the overall ground state

(*i.e.*, E^0, with all molecules in S_0, no photon in the cavity: $|S_0^1 S_0^2 ... S_0^N\rangle|0\rangle$) were extracted, multiplied by $|\alpha^m|^2$ and summed up into a superposition of Gaussian functions:

$$I^{\text{abs}}(E) \propto \sum_{i}^{s} \left[\sum_{m}^{N+n_{\text{max}}+1} |\alpha_i^m|^2 \exp[-\frac{(E-\Delta E_i^m)^2}{2\sigma^2}] \right] \tag{S.20}$$

Here, $I^{\text{abs}}(E)$ is the absorption intensity as a function of excitation energy E, s the number of trajectory frames included in the analysis, ΔE_i^m the excitation energy of polaritonic state $|\psi^m\rangle$ in frame i ($\Delta E_i^m = E_i^m - E_i^0$) and α_i^m the expansion coefficient of the cavity mode in polaritonic state $|\psi^m\rangle$ in that frame (Equation S.13). A width of $\sigma = 0.05$ eV was chosen for all convolutions in this work.

2.6 Overlap between molecular polaritonic states

The density of states (DOS) of the bare HBQ in cyclohexane was determined by convoluting the distribution of the 2,048 QM/MM excitation energies with a Gaussian function:

$$p_{\text{mol}}^{\text{DOS}}(E) = \sum_{i}^{s} \Delta E_i \exp[-\frac{(E-\Delta E_i)^2}{2\sigma^2}] \tag{S.21}$$

where E is the excitation energy, $s = 2048$ and we again use $\sigma = 0.05$ eV. Because polaritonic states are characterized by a non-zero photonic contribution (*i.e.* $|\alpha^k|^2 > 0$, Equation S.13) the DOS of these polaritonic states was calculated by weighing all polaritonic states by their photonic contribution:

$$p_{\text{pol}}^{\text{DOS}}(E) = \sum_{i}^{S} \left[\sum_{k}^{N+1} (E_i^k - E_i^0) \exp[-\frac{(E-(E_i^k - E_i^0))^2}{2\sigma^2}] |\alpha_i^k|^2 \right] \tag{S.22}$$

where subscript i indicates the value of the parameter in snapshot i. To estimate the overlap between the DOS of the lower polariton and the DOS of the molecules, we fitted Gaussian functions to the DOS profiles of equations S.21 and S.22. A single Gaussian was used to fit $p_{\text{mol}}^{\text{DOS}}(E)$ while $p_{\text{pol}}^{\text{DOS}}(E)$ was fitted with a sum of two Gaussians. The overlap integral between the fits to the molecular and polaritonic DOS was then calculated analytically.

2.7 Additional MD results

2.7.1 ESIPT in "bare" HBQ

We performed 100 TDA-CAM-B3LYP/6-31G(d)//Gromos-2016H66 QM/MM MD simulations of HBQ in cyclohexane without a cavity, *i.e.*, *bare* HBQ. The starting structures were selected at 0.5 ps intervals from the ground-state CAM-B3LYP/6-31G(d)//Gromos-2016H66 equilibrium trajectory and instantaneously excited into the S_1 electronic state. In figure S7 we plot the distance between the hydroxyl oxygen and hydroxyl hydrogen as a function of time for all simulations. In all simulations, the intra-molecular proton transfer took place within 100 fs with an average reaction time, defined as the time at which the distance between the oxygen and hydrogen exceeds 0.125 nm, of 0.44 fs.

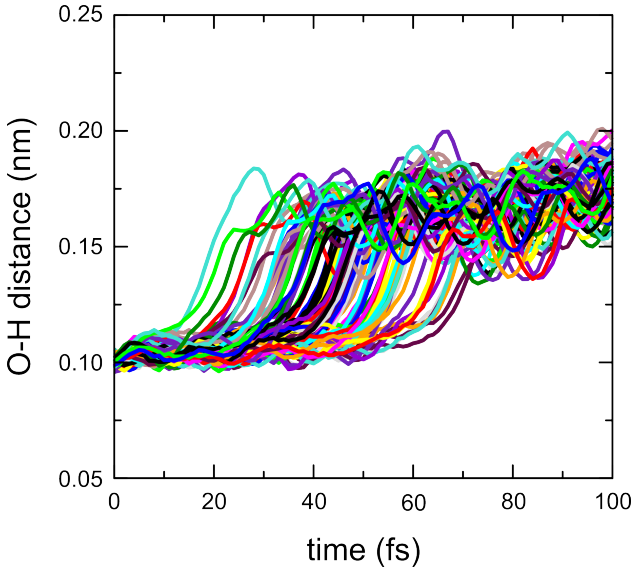

Fig. S7. Distance between the Oxygen and Hydrogen atoms for 100 QM/MM trajectories (all colours) of HBQ in cyclohexane as a function of time after instantaneous excition into the S_1 electronic state.

2.7.2 ESIPT in HBQ under strong light-matter coupling

Tables 1-3 provide an overview of the results of MD simulations with 512 and 256 molecules in a single-mode cavity. In all simulations, proton transfer occurred, and the average quantum yields, $\eta^{\text{sim.}}$ defined as the population in the product state at the end of the simulation (Equation S.19, last column in Tables 1-3), were 95% for 512 HBQ molecules in a tuned cavity, 86% for the 512 HBQ molecules in a red-detuned cavity, and 91% for 256 HBQ molecules in a tuned cavity.

Table 1: Simulation results for 512 HBQ molecules in a *tuned* single-mode cavity, with parameters: $\hbar\omega_{\text{cav}} = 4.01$ eV, $\sqrt{\hbar\omega_{\text{cav}}/2\epsilon_0 V_{\text{cav}}} = 0.77$ MVcm^{-1}, and $\gamma_{\text{cav}} = 250$ ps^{-1}

$\|\psi^m\rangle$	$\|\alpha^m\|^2$	t^{ESIPT}	molecule	$\eta^{\text{sim.}}$
0	0.0008	48 fs	404	0.97
19	0.026	25 fs	400	0.97
26	0.022	36 fs	254	0.96
27	0.019	37 fs	254	0.95
29	0.011	33 fs	484	0.95
31	0.008	36 fs	312	0.95
32	0.018	35 fs	312	0.96
36	0.014	34 fs	340	0.95
40	0.015	27 fs	194	0.95
46	0.013	29 fs	384	0.95
63	0.001	58 fs	495	0.98
95	0.0001	60 fs	173	0.96
127	0.0006	16 fs	179	0.98
159	$4\ 10^{-5}$	27 fs	138	0.95
191	$3\ 10^{-6}$	52 fs	394	0.97
223	0.0002	56 fs	306	0.94
255	0.0005	54 fs	450	0.96
450	0.017	26 fs	120	0.94
485	0.044	41 fs	368	0.93
486	0.039	58 fs	422	0.96
494	0.036	43 fs	278	0.93
512	0.0006	56 fs	131	0.94

Table 2: Simulation results for 512 HBQ molecules in a *detuned* single-mode cavity, with parameters: $\hbar\omega_{\text{cav}} = 3.90$ eV, $\sqrt{\hbar\omega_{\text{cav}}/2\epsilon_0 V_{\text{cav}}} = 0.77$ MVcm^{-1}, and $\gamma_{\text{cav}} = 250$ ps^{-1}

$\|\psi^m\rangle$	$\|\alpha^m\|^2$	t^{ESIPT}	molecule	$\eta^{\text{sim.}}$
2	0.19	21 fs	5	0.79
4	0.12	11 fs	212	0.82
5	0.13	23 fs	167	0.80
7	0.03	52 fs	331	0.92
11	0.02	12 fs	35	0.93
14	0.02	94 fs	396	0.86
15	0.03	75 fs	67	0.92

Table 3: Simulation results for 256 HBQ molecules in a *tuned* single-mode cavity, with parameters: $\hbar\omega_{\mathrm{cav}} = 4.01$ eV, $\sqrt{\hbar\omega_{\mathrm{cav}}/2\epsilon_0 V_{\mathrm{cav}}} = 0.77$ MVcm^{-1}, and $\gamma_{\mathrm{cav}} = 250$ ps^{-1}

$\lvert\psi^m\rangle$	$\lvert\alpha^m\rvert^2$	t^{ESIPT}	molecule	$\eta^{\mathrm{sim.}}$
17	0.027	53 fs	209	0.95
27	0.033	85 fs	110	0.90
36	0.022	26 fs	200	0.89
51	0.017	49 fs	102	0.93
55	0.022	59 fs	191	0.92
66	0.011	25 fs	77	0.90
69	0.015	12 fs	137	0.89
132	0.016	25 fs	77	0.90
146	0.018	33 fs	118	0.91
165	0.037	51 fs	29	0.90
167	0.038	77 fs	249	0.90
170	0.014	30 fs	235	0.94
183	0.0156	20 fs	92	0.90
188	0.011	59 fs	191	0.91
192	0.029	66 fs	85	0.90
196	0.011	69 fs	46	0.91
197	0.011	76 fs	9	0.90
204	0.011	71 fs	54	0.90
205	0.020	70 fs	65	0.95
223	0.020	54 fs	58	0.92
241	0.013	25	19	0.90

2.8 Reference Potential Energy Surfaces of HBQ molecule

First, we computed the potential energy surfaces (PES) of HBQ molecule on ground ($S0_1$) and excited (S_1) states using TPSSh/cc-pVDZ level of theory. To reproduce the results of Picconi [S39], we performed relaxed surface scans on both states, while constraining the reaction coordinate, defined as $RC = d_{\text{O-H}} - d_{\text{N-H}}$ in Ångström (see Figure S8). Results of that scan are plotted as dashed lines with open circels in Figure S8. At this level of theory proton transfer is barrierless in the excited state. From the S_0 and S_1 minima excitation and fluorescence peaks have been calculated: 3.13 eV (396 nm) and 2.29 eV (541 nm), respectively.

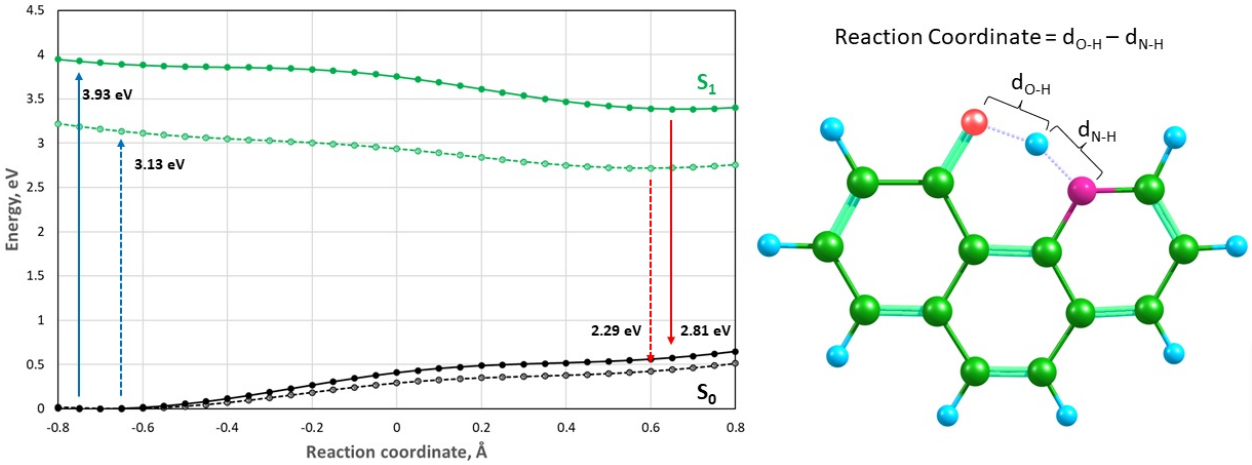

Fig. S8. Potential energy surface are shown on the left panel: solid lines for CAM-B3LYP/cc-pVDZ and dashed lines for TPSSh/cc-pVDZ levels of theory. Reaction coordinate used for relaxed scans are shown on the right panel.

While the TPSSh functional shows very good results for HBQ molecule, the lack of that functional in TeraChem quantum chemistry package [S34, S35] forced us to search for qualitatively similar functional that can reproduce the barrierless character of the intramolecular proton transfer reaction. We found that the CAM-B3LYP/cc-pVDZ level of theory (solid lines on Figure S8) suited our purposes, despite an overestimation of both the excitation and fluorescence energies: 3.93 eV (315 nm) and 2.81 eV (441 nm).

2.9 Simulations in Ultra-Strong Coupling Regime

In the ideal situation, in which all HBQ molecules are identical and the mirrors of the single-mode cavity are perfect, two bright polaritons and $N-1$ degenerate states form, irrespective of the coupling strength (provided it is not zero) and the ratio $N_{\text{dark}}/N_{\text{pol}} = (N-1)/2$ for all Rabi splittings. In contrast, when there is thermal disorder, the cavity modes are smeared-out over many eigenstates [S40–S42]. In this situation, there is no longer a clear distinction between dark and polaritonic states. Instead, we applied a numerical criterion and consider a state $|\psi^m\rangle$ polaritonic if the total cavity mode contribution to that state exceeds a threshold *i.e.*, $|\alpha^m|^2 \geq 0.01$.

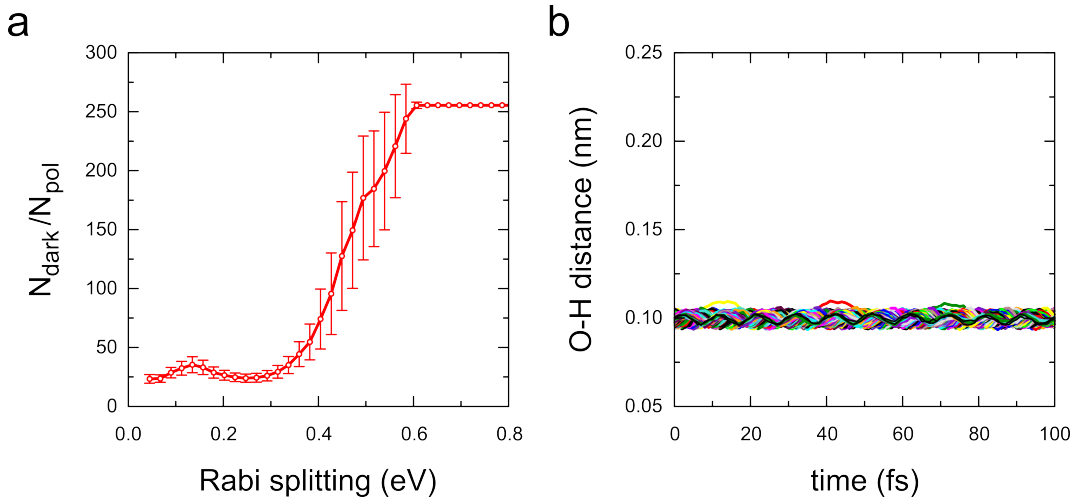

Fig. S9. Panel a shows the ratio between the dark and polaritonic states ($N_{\mathrm{dark}}/N_{\mathrm{pol}}$) as a function of Rabi splitting for a disordered ensemble of 512 molecules collectively coupled to a single cavity mode that is resonant with the molecular excitation energy (4.01 eV) and a threshold of $\epsilon = 0.01$. Panel b shows the distance between the hydroxyl oxygen atom and hydroxyl hydrogen atom in 512 HBQ molecules after excitation into the lower polariton with a cavity vacuum field strength of 1.92 MVcm^{-1} (0.000375 au), which yields a Rabi splitting of $\hbar\Omega^{\mathrm{Rabi}} = 0.64$ eV.

In Fig. S9a we plot the ratio between the dark and polaritonic states of 512 HQB molecules in the single-mode cavity as a function of the Rabi splitting, or equivalently the coupling strength. In these calculations, we controlled the coupling strength by varying the cavity mode volume (V_{cav}, Equation S.3). To account for the thermal disorder among the molecules, we randomly selected 1000 different sets of 512 energies plus transition dipole moments from the QM/MM equilibrium trajectory at 300 K for each coupling strength.

For Rabi splittings exceeding 0.6 eV, the ratio becomes "ideal" (*i.e.*, $N_{\mathrm{dark}}/N_{\mathrm{pol}} = (N-1)/2 = 253.5$, and the UP and LP polaritons are coherent hybrids of *all* molecular excitations and the cavity mode excitation. Indeed, at a Rabi splitting of 0.64 eV, no proton transfer was observed in a simulation initiated in the LP state (Fig. S9b). However, because the Rabi splitting is larger than 10% of the excitation energy, the system is in the Ultra Strong Coupling regime [S43]. In this regime, the Rotating Wave Approximation (RWA), on which our simulation model is based, may no longer be strictly valid [S44, S45]. Nevertheless, the results of the analysis and simulations suggest that for typical organic molecules, ultra-strong coupling conditions is required to suppress photo-reactivity.

References

S1. Mackay, T. G. & Lakhtakia, A. *The Transfer-Matrix Method in Electromagnetics and Optics* (Morgan and Claypool, San Rafael, 2020).

S2. Pascoe, K. J. *Reflectivity and Transmissivity through Layered, Lossy Media: A User-Friendly Approach* (Wright Patterson Air Force Base, Ohio, 2001).

S3. Gedney, S. *Introduction to the Finite-Difference Time-Domain (FDTD) Method for Electromagnetics* (Morgan and Claypool, San Rafael, 2011).

S4. `https://www.ansys.com/products/photonics/fdtd`.

S5. Palik, E. D. *Handbook of Optical Constants of Solids* (Academic, Burlington, 1997).

S6. Dutta, A., Tiainen, V. & Toppari, J. J. Optimizing geometry of low-Q all-metal Fabry-Pérot microcavity for fluorescence spectroscopy. *IOP SciNotes* **2,** 015205 (2021).

S7. `https://www.mathworks.com/products/matlab.html`.

S8. `https://www.mathworks.com/help/matlab/ref/interp1.html`.

S9. `https://www.mathworks.com/help/matlab/ref/pchip.html`.

S10. Kavokin, A. V., Sheremet, A. S., Shelykh, I. A., Lagoudakis, P. G. & Rubo, Y. G. Exciton-photon correlations in bosonic condensates of exciton-polaritons. *Sci. Rep.* **5,** 12020 (2015).

S11. Hertzog, M., Wang, M., Mony, J. & Börjesson, K. Strong light–matter interactions: a new direction within chemistry. *Chem. Soc. Rev.* **48,** 937–961 (2019).

S12. Baieva, S. *Interaction between surface plasmon polaritons and molecules in strong coupling limit* (University of Jyväskylä, PhD Dissertation, 2016).

S13. Jaynes, E. T. & Cummings, F. W. Comparison of quantum and semiclassical radiation theories with to the beam maser. *Proc. IEEE* **51,** 89–109 (1963).

S14. Tavis, M. & Cummings, F. W. Approximate solutions for an N-molecule radiation-field Hamiltonian. *Phys. Rev.* **188,** 692–695 (1969).

S15. Luk, H.-L., Feist, J., Toppari, J. J. & Groenhof, G. Multiscale Molecular Dynamics Simulations of Polaritonic Chemistry. *J. Chem. Theory Comput.* **13,** 4324–4335 (2017).

S16. Warshel, A. & Levitt, M. Theoretical studies of enzymatic reactions: Dielectric, electrostatic and steric stabilization of carbonium ion in the reaction of lysozyme. *J. Mol. Biol.* **103,** 227–249 (1976).

S17. Boggio-Pasqua, M., Burmeister, C. F., Robb, M. A. & Groenhof, G. Photochemical reactions in biological systems: probing the effect of the environment by means of hybrid quantum chemistry/molecular mechanics simulations. *Phys. Chem. Chem. Phys.* **14,** 7912–7928 (2012).

S18. Crespo-Otero, R. & Barbatti, M. Recent Advances and Perspectives on Nonadiabatic Mixed Quantum-Classical Dynamics. *Chem. Rev.* **118,** 7026–7068 (2018).

S19. Groenhof, G. *et al.* Photoactivation of the photoactive yellow protein: Why photon absorption triggers a trans-to-cis isomerization of the chromophore in the protein. *J. Am. Chem. Soc* **124,** 4228–4232 (2004).

S20. Landau, L. Zur theorie der energieubertragung. II. *Phys. Z. Sowjetunion* **2,** 1–13 (1932).

S21. Zener, C. Non-adiabatic crossing of energy levels. *Proc. R. Soc. A* **137,** 696–702 (1932).

S22. Desouter-Lecomte, M. & Lorquet, J. Nonadiabatic interactions in unimolecular decay. IV. Transition probability as a function of the Massey parameter. *J. Chem. Phys.* **71,** 4391–4403 (1979).

S23. Hammes-Schiffer, S. & Tully, J. C. Proton transfer in solution: molecular dynamics with quantum transitions. *J. Chem. Phys.* **101,** 4657–4667 (1994).

S24. Horta, B. A. C. *et al.* A GROMOS-Compatible Force Field for Small Organic Molecules in the Condensed Phase: The 2016H66 Parameter Set. *J. Chem. Theory. Comput.* **12,** 3825–3850 (2016).

S25. Hess, B., Bekker, H., Berendsen, H. J. C. & Fraaije, J. G. E. M. LINCS: A linear constraint solver for molecular simulations. *J. Comput. Chem.* **18,** 1463–1472 (1997).

S26. Berendsen, H., Postma, J., van Gunsteren, W., la, A. D. & Haak, J. Molecular dynamics with coupling to an external bath. *J. Chem. Phys.* **81,** 3684–3690 (1984).

S27. Becke, A. D. A new mixing of Hartree-Fock and local density-functional theories. *J. Chem. Phys.* **98,** 1372 (1993).

S28. Lee, C. T., Yang, W. T. & Parr, R. G. Development of the Colle-Salvet correlation-energy formula into a functional of the electron density. *Phys. Rev. B* **37,** 785–789 (1988).

S29. Yanai, T., Tew, D. P. & Handy, N. C. A new hybrid exchange-correlation functional using the Coulomb-attenuating method (CAM-B3LYP. *Chem. Phys. Lett.* **393,** 51–57 (2004).

S30. Dunning, T. H. Basis Functions for Use in Molecular Calculations. I. Contractions of (9s5p) Atomic Basis Sets for the First-Row Atoms. *J. Chem. Phys.* **53,** 2823–2833 (1970).

S31. Runge, E. & Gross, E. K. U. Density-Functional Theory for Time-Dependent Systems. *Phys. Rev. Lett* **52,** 997–1000 (1984).

S32. Hirata, S. & Head-Gordon, M. Time-dependent density functional theory within the Tamm–Dancoff approximation. *Chem. Phys. Lett.* **314,** 291–299 (1999).

S33. Hess, B., Kutzner, C., van der Spoel, D. & Lindahl, E. GROMACS 4: Algorithms for Highly Efficient, Load-Balanced, and Scalable Molecular Simulation. *J. Chem. Theory Comput.* **4,** 435–447 (2008).

S34. Ufimtsev, I. & Martínez, T. J. Quantum Chemistry on Graphical Processing Units. 3. Analytical Energy Gradients and First Principles Molecular Dynamics. *J. Chem. Theory Comput.* **5,** 2619–2628 (2009).

S35. Titov, A., Ufimtsev, I., Luehr, N. & Martínez, T. J. Generating Efficient Quantum Chemistry Codes for Novel Architectures. *J. Chem. Theory Comput.* **9,** 213–221 (2013).

S36. Frisch, M. J. *et al. Gaussian˜16 Revision C.01* Gaussian Inc. Wallingford CT. 2016.

S37. Granucci, G., Persico, M. & Toniolo, A. Direct semiclassical simulation of photochemical processes with semiempirical wave functions. *J. Chem. Phys.* **114,** 10608–10615 (2001).

S38. Lidzey, D., Bradley, D., Armitage, A., Walker, S. & Skolnick, M. Photon-Mediated Hybridization of Frenkel Excitons in Organic Semiconductor Microcavities. *Science* **288,** 1620–1623 (2000).

S39. Picconi, D. Nonadiabatic quantum dynamics of the coherent excited state intramolecular proton transfer of 10-hydroxybenzo [h] quinoline. *Photochemical & Photobiological Sciences* **20,** 1455–1473 (2021).

S40. Houdré, R., Stanley, R. P. & Ilegems, M. Vacuum-field Rabi splitting in the presence of inhomogeneous broadening: Resolution of a homogeneous linewidth in an inhomogeneously broadened system. *Phys. Rev. A* **53,** 2711–2715 (1996).

S41. Groenhof, G., Climent, C., Feist, J., Morozov, D. & Toppari, J. J. Tracking Polariton Relaxation with Multiscale Molecular Dynamics Simulations. *J. Chem. Phys. Lett.* **10,** 5476–5483 (2019).

S42. Mony, J., Climent, C., Anne Ugleholdt Petersen Kasper Moth-Poulsen, J. F. & Börjesson, K. Photoisomerization Efficiency of a Solar Thermal Fuel in the Strong Coupling Regime. *Adv. Funct. Mater.* **31,** 2010737 (2021).

S43. Forn-Díaz, P., Lamata, L., Rico, E., Kono, J. & Solano, E. Ultrastrong coupling regimes of light-matter interaction. *Rev. Mod. Phys.* **91,** 025005 (2019).

S44. Flick, J., Ruggenthaler, M., Appel, H. & Rubio, A. Cavity Born-Oppenheimer Approximation for correlated Electron-Nuclear-Photon Systems. *J. Chem. Theory Comput.* **13,** 1616–1625 (2017).

S45. Flick, J., Ruggenthaler, M., Appel, H. & Rubio, A. Atoms and Molecules in Cavities: From Weak to Strong Coupling in QED Chemistry. *Proc. Natl. Acad. Sci. USA* **114,** 3026–3034 (2017).